Graphitic Nanostructure integrated NiO Composites for High-Performance Lithium-ion Batteries

Niranjala Fernando[†], Harikishan Kannan[‡], Francisco C Robles Hernandez[‡, §], Pulickel M. Ajayan[‡], Ashokkumar Meiyazhagan[‡, *], Amor Abdelkader [†,*]

[†]Faculty of Science and Technology, Bournemouth University, Poole House, Talbot Campus, Poole, Dorset BH12 5BB

[‡] Department of Materials Science & NanoEngineering, 6100 Main Street, Rice University, Houston, TX, 77005, United States

[‡, §] College of Engineering Technology, University of Houston, Houston, TX, 77204-4020, United States

* *Corresponding authors E-mail:* ma37@rice.edu and aabdelkader@bournemouth.ac.uk

ABSTRACT

So far, various graphite-Nickel Oxide (NiO) composites have been investigated as anodes for Li-ion batteries. However, developing an ideal composite that overcomes NiO's electrical conductivity limitations remains a significant challenge. The current study presents an in-situ one-step hydrothermal technique for integrating NiO into a 3D peony-like graphitic nanostructure (NiO-GNF), resulting in unique thin nanosheet arrays with porous, conductive channels. Notably, the composites endowed controlled aggregation and restacking of NiO, buffered electrode stress and improved electrical conductivity due to the expanded nature of graphite. In addition, the enlarged interlayer spacing of expanded graphite facilitated an improved Li-ion insertion. Overall, in comparison to pure NiO anodes, the NiO-GNF composite achieved an impressive electrochemical improvement exhibiting a highly reversible discharge capacity of 678.2 mAh/g after 370 cycles at a current density of 0.5 A g^{-1}, corresponding to a capacity retention of 60.7 %. The composite also demonstrated a capacity of 752 mAh/g at a high current density of 1.2 A g^{-1}.

Keywords: Expanded graphite nanoplatelets, NiO-hybrids anodes, high-capacity anode, Li-ion batteries

INTRODUCTION

Lithium-ion batteries (LIBs) are considered as one of the most promising power sources for mobile, portable electronics, and electric vehicles (EVs) due to their excellent energy efficiency, high cell potential, low cost, and long cycle life. However, the commercial graphite used in LIBs is insufficient to meet the current market demands owing to a limited theoretical capacity of ~ 372 mAh g^{-1}.[1] As potential high energy substitutes; transition metal oxides (TMOs), such as Co, Ni, Fe, Cu, Ti, and Zn oxides and their composites, have garnered research attention due to their exceptional storage capacity and high energy density of approximately 700 mAh g^{-1}, according to the equation of $MO + 2Li^+ + 2e = M + Li_2O$.[2-8] Amongst metal oxides, nickel oxide (NiO) is highly appealing as a promising anode for LIBs due to their abundance, low cost, eco-benignity, admirable safety, and high volumetric energy density.[9] However, pristine NiO utilization, as for other oxides, significantly failed as an effective anode for LIBs due to their poor electrical conductivity, low rate performance, and limited cyclability.[10]

One effective protocol used in the literature is combining NiO with carbon nanostructures. A carbon-based composite design not only provides more surface area but also offers increased electrical conductivity and desirable mechanical flexibility that buffers the volume expansion of NiO. Various carbonaceous matrices have been extensively studied, including graphite, graphene, hard carbon, carbon nanofibres, and carbon nanotubes.[10-21] For instance, Li *et al.* have revealed that the capacity and capacity retention of pristine NiO can be significantly enhanced by incorporating them into the graphene matrix. This approach leads to the formation of flower-like nickel oxide/reduced graphene oxide (NiO/RGO) nanocomposite, which can exhibit a specific storage capacity of 702.3 mAh/g and capacity retention of 77.0 % after 100 cycles at a current density of 0.1 A g^{-1}. Similarly, Shi *et al.*

developed a 3D graphene/NiO nanobelt composite, which significantly enhanced graphene's volumetric and specific capacities by 75 and 41%, respectively. The composite formed displayed a cycling life of 360 cycles, and a specific capacity of 445 mAh/g at a high current density of 2 A g^{-1}.[12] An exciting research by Park *et al*. explored coaxial carbon nanofiber/NiO core-shell nano cables with an outstanding reversible capacity of 825 mAh g^{-1} at a current density of 0.2 A g^{-1}.[13] Further, Shao and co-authors developed a freestanding NiO/Graphene form anode composite, which exhibited a capacity of 640 mAh g^{-1} after 50 cycles at 100 mA g^{-1} and an excellent rate capability of 330 mAh g^{-1} at a current density of 1 A g^{-1}.The authors claimed that the outstanding electrochemical performance of the composite is a result of the synergistic effect between the NiO and graphene form (GF) components. The graphene form not only enhance the electrical conductivity but also act as a flexible substrate for NiO and prevent the diffusion of NiO particles into the electrolyte during cycling. Moreover, the unique hierarchical hollow structure of NiO effectively reduces the electrode stress by controlling the volume change.[22]

Despite many efforts in the design of NiO/ carbonaceous composites, several challenges remain in developing an ideal composite to solve issues such as conductivity and synthesis procedures. For example, the graphene/NiO composites synthesis processes require several steps, raising questions about the scalability and practicality of the materials. Another issue described in the literature is decoupling the composite components during the cycling process of Li-ion with graphene and NiO. The oxide nanoparticles tend to aggregate into clusters with high local impedance after a few cycles, leading to a substantial decline in capacity.

In this work, we introduce a nanocomposite anode of NiO on a 3D carbon network produced by expanding graphite into nanoflowers (NiO-GNF). The synergy between NiO and the conductive carbon platform significantly improved the anode performance in Li-ion batteries. Firstly, the 3D carbon nanoflower backbone provided a large surface area and

94 excellent conductivity to the active materials. Secondly, the NiO partially intercalated into the
95 graphite gallery, expanding the interlayer lattice distance and promoting faster Li^+ transport
96 and larger storage capacity. Thirdly, the well-designed nanoflower structure buffered the
97 volumetric changes during the charge and discharge, significantly improving the cycle life,
98 which was investigated in detail.

99 **RESULTS AND DISCUSSION**

100

101 A schematic illustration of the proposed mechanism for the NiO-GNF is displayed in Figure
102 1a. This work used nickel salt and bulk graphite powders as raw materials to derive nickel-
103 encapsulated expanded graphite. In the first step, during the hydrothermal reaction, nickel,
104 sodium, and citrate ions intercalate into the bulk graphite matrix to derive an intercalated
105 graphite compound (GIC). Next, the gaseous substances trapped between the graphitic layers
106 are released progressively, due to which the interlayer spacing between the sheets increases.
107 The vigorous hydrothermal conditions and continuous *in-situ* gas formation further weaken the
108 Van der Waals forces, resulting in exfoliated graphitic nanosheet formation. Simultaneously,
109 the nickel ions in the hydrothermal chamber nucleate and grow to form Ni nanostructures
110 within the graphite sheets resulting in Ni intercalated expanded graphitic nanostructures.
111 Moreover, the formation of expanded graphite particles effectively prevents the aggregation of
112 Ni nanostructures due to steric hindrance. The formed composite indicates nest-like structures
113 after synthesis (**Figure S1**). However, the morphology transformed into peony-like 3D
114 structures following heat treatment, which might be due to the conversion of hydroxide to
115 oxides and the removal of various gases during the process.

116 X-ray diffraction (XRD), exhibited in **Figure S2,** and resembles NiO. The diffraction
117 peaks located at 2-Theta 37.2º, 43.3º, and 62.8º corresponds to (111), (200), and (220) planes

of cubic NiO, respectively (JCPDS 73-1523). [23]The inter-planer spacing (d-spacing) of 0.24 nm was observed for the peak at 43.3˚. In addition, the NiO-GNF nanocomposite (**Figure S3**) displayed additional peaks at 26.4˚and 54.23° attributed to the graphitic backbone (JCPDS 01-0640).[24] Raman spectroscopic analysis also confirms the presence of the NiO phase in the NiO-GNF composite. As seen in **Figure S4,** two significant peaks can be observed for the petal of a peony-like structure, a prominent peak at ~ 500 cm^{-1} and a broad peak at around 1062 cm^{-1} corresponding to NiO first (1P) and second-order phonon (2P) scattering respectively.[25]

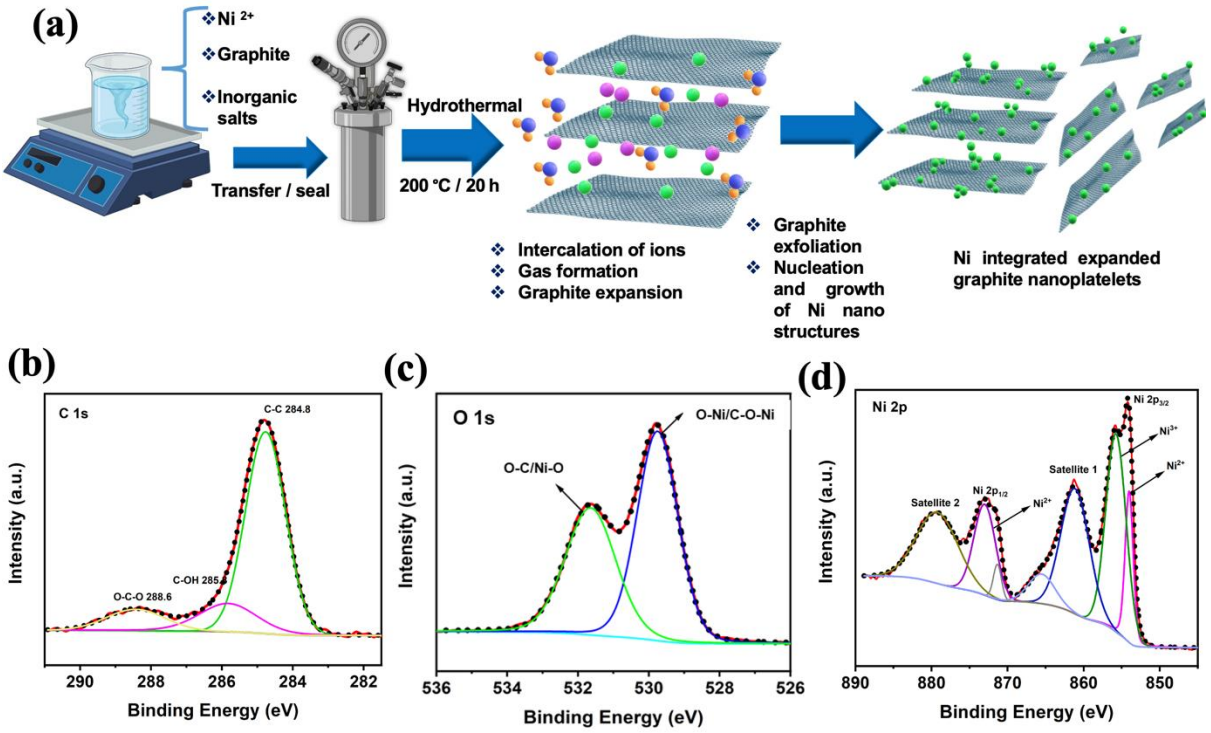

Figure 1. Synthesis and characterization of NiO/GNF. (a) Schematic illustration of peony-like 3D architecture formation using nickel salt and bulk graphite powders as raw materials to derive nickel-encapsulated expanded graphite. During the hydrothermal reaction, nickel, sodium, and citrate ions intercalate into the bulk graphite matrix to derive an intercalated graphite compound. The hydrothermal treatment and continuous *in-situ* gas formation weaken the Van der Waals forces, resulting in Ni-integrated expanded graphite nanoplatelets.

Deconvoluted XPS spectra of (b) C 1s, (c) O 1s, and (d) Ni 2p confirm the chemical valence states of the NiO/GNF composite.

X-ray photoelectron spectroscopy (XPS) was carried out to confirm the chemical valence states of the NiO/GNF composite and to understand their elemental compositions (**Figure 1b-d**). XPS survey spectrum shown in **Figure S5** verifies the presence of carbon (C), nickel (Ni), and oxygen (O). **Figure 1b** displays the C1s spectrum with binding energy at 284.8 eV corresponding to sp^2-hybridized carbon (C–C bond). Additionally, two low-intensity peaks can be detected at ~285 and 288 eV, corresponding to the sp^3 hybridized C–OH and O-C-O bonds.[26] The O1s spectrum exhibits two significant peaks at 529.4 and 531.7 eV, which can be ascribed to the metal-oxygen bonds such as O-Ni /C–O–Ni and the O-C/Ni-O respectively (**Figure 1c).** The results of the C1s and O1s peaks suggested the link between NiO and the graphitic backbone goes beyond the simple physical or chemical adsorption due to strong chemical bonds.[27, 28] The Ni2p spectrum experiences two-edge splits due to spin-orbital coupling (**Figure 1d)**. The binding peaks observed at ~854 and ~872 eV and their satellite peaks at ~862 and ~879 can be attributed to the respective $2p_{3/2}$ and Ni $2p_{1/2}$ spin-orbit levels of NiO. Additional shoulder peak at ~ 855 eV might be due to surface oxidation of NiO to Ni_2O_3.

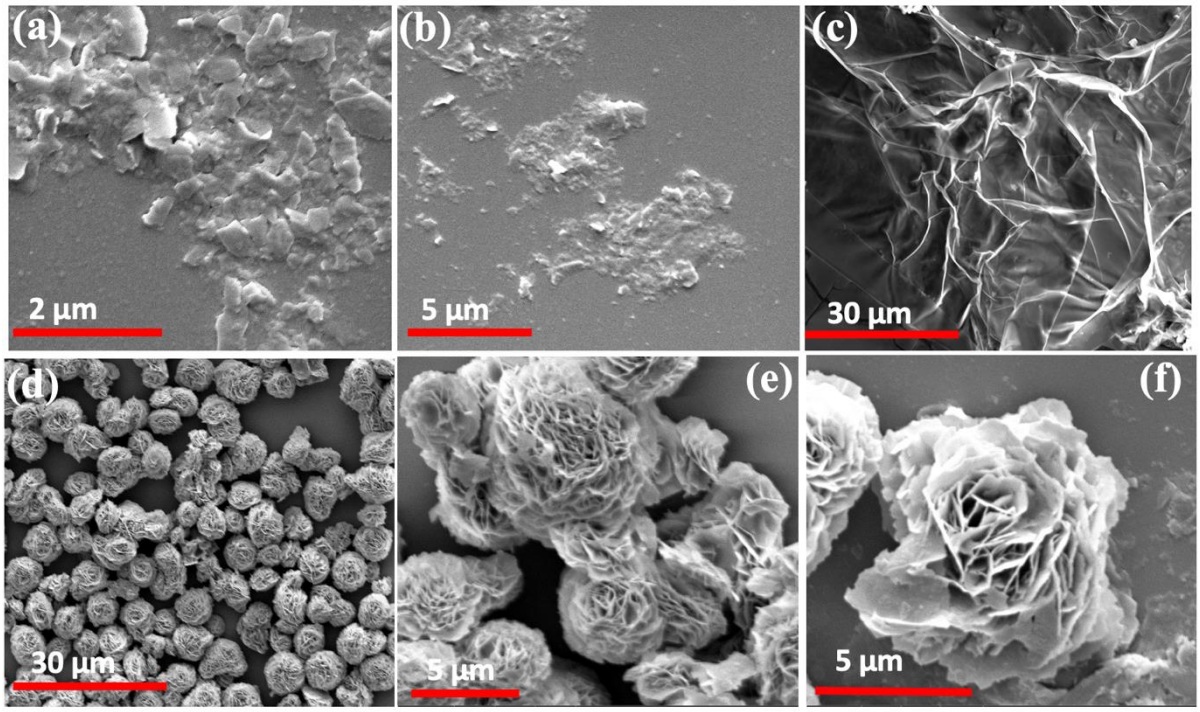

Figure 2. SEM images: **(**a and b) bulk NiO/graphite powders before hydrothermal treatment showing bulk particles and flakes, (c-f) corresponds to samples derived after hydrothermal process where (c) displays crumpled thin nano-sheet, and (d-f) higher magnification NiO-GNF composite material displaying an interconnected petal morphology with uniform distribution of exfoliated EG sheets encapsulated with NiO.

Figure 2 shows scanning electron microscope (SEM) images of the bulk NiO/graphite powders before and after hydrothermal and calcination steps. The hydrothermal process significantly altered the surface morphologies displaying the crumpled thin nano-sheet morphology of expanded graphite **(Figure 2c)**. Similarly, NiO-GNF composite experiences highly porous peonies-like reticulation, as illustrated in **Figure 2 d-f**. A detailed look through higher magnification SEM (**Figure 2e&f**) reveals an interconnected petal morphology with uniform distribution of exfoliated EG sheets over the petals. This observation indicates the simultaneous occurrence of Ni nanostructures nucleation and the slow release of gaseous substances during the hydrothermal process transforming the bulk powders into highly ordered

NiO-encapsulated GNF structures. The presence of carbon, Ni, and O was re-validated through SEM/EDX mapping **(Figure S6).** Furthermore, the NiO percentage in the NiO-GNF composite was calculated as 61.98 wt. %. (See TGA interpretation, **Figure S8**). Compared with pristine NiO, NiO-GNF composite could lead to uniform conductivity, thereby modulating NiO's electrical resistance behavior during the Li-ion battery electrochemical performance.

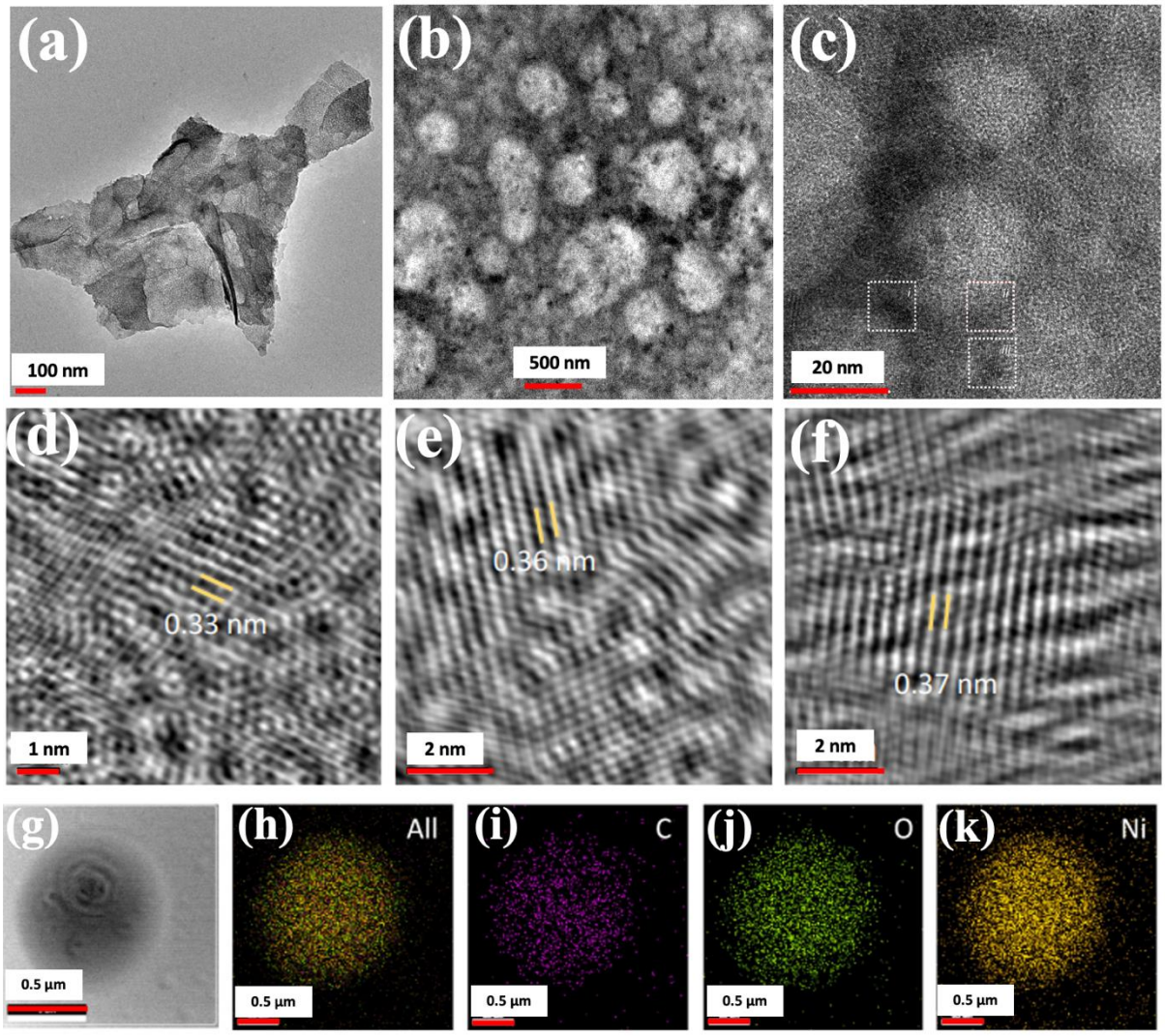

Figure 3. TEM image of derived samples (a) exfoliated graphene sheets; (b) displays the presence of scattered NiO nanoparticles (c) displays *d-spacing* values taken at three different regions (marked i, ii, and iii) correspond to differences in interlayer spacings at various spots where (d) show 0.33 nm, (e) 0.36 nm and (f) 0.37 nm. TEM-EDS mapping area is shown in

(g), and (h) shows the presence of all expected elements where (i) corresponds to carbon, (j) oxygen, and (k) nickel.

Transmission electron microscopy (TEM) (**Figure 3a-k)** was carried out to understand the peeling of bulk graphite into thin expanded graphite nanoplatelets during the hydrothermal process. **Figure 3a** displays the stacking of multilayer expanded graphite sheets, and **figure 3b** shows the presence of scattered NiO particles with white patch-like morphology. To confirm the expanded graphite formation, we measured *d-spacing* at three different regions (**Figure 3c inset**) and identified the following values: (i) 0.33, (ii) 0.36, and (iii) 0.37 nm. These reflections are typical of morphed graphene corresponding to (110) planes which agrees with the XRD peak observed ~26^{o} (2θ). The increase in the interlayer spacing could be attributed to layer expansion during the hydrothermal treatment and the subsequent calcination step. Similarly, the high-resolution transmission electron microscopy (HRTEM) image of NiO particles (Figure S7) displays lattice fringes with interplanar spacing of 0.26 nm and 0.2 nm, corresponding to (111) and (200) crystal planes, respectively. [29] The NiO-GNF samples were further characterized through TEM-EDS mapping to confirm the presence of different elements, and the results are shown in (**Figure 3g-k**). As seen, the TEM-EDS results display uniform distribution of C, Ni, and O elements, confirming the possibility of transforming bulk graphitic structures to few-layered graphene sheets encapsulated with NiO.

It is well-known that surface area and pore hierarchy of material plays a significant role in the Li-ion transport phenomenon. Therefore, we carried out nitrogen adsorption-desorption analysis to measure the changes in surface area and pore size distribution of NiO-GNF composite and pristine NiO. Both materials displayed typical type IV isotherm curves, indicating the presence of mesoporous features. However, the NiO-GNF sample revealed multistage pore size distribution showing the presence of micro, meso, and macro pores for composites, while the NiO is predominantly microporous (< 2 nm). The micropores probably

arise due to the loss of several organic O and H species during the hydrothermal treatment, while graphene sheets contribute to mesopore formations. The total pore volume, average pore diameter, and specific surface area of NiO-GNF were 0.33 $cm^3\ g^{-1}$, 7.29 nm, and 178 $m^2\ g^{-1}$, respectively, and for the pristine sample, it was 0.13 $cm^3 g^{-1}$, 6.06 nm, and 82.9 $m^2\ g^{-1}$ respectively. **(Figure S9)**. The multistage size distribution and higher surface area of NiO-GNF suggest enhanced Li-ion migration and comparatively higher Li-ion storage capacity, which is favorable for fabricating high-capacitive energy storage material.

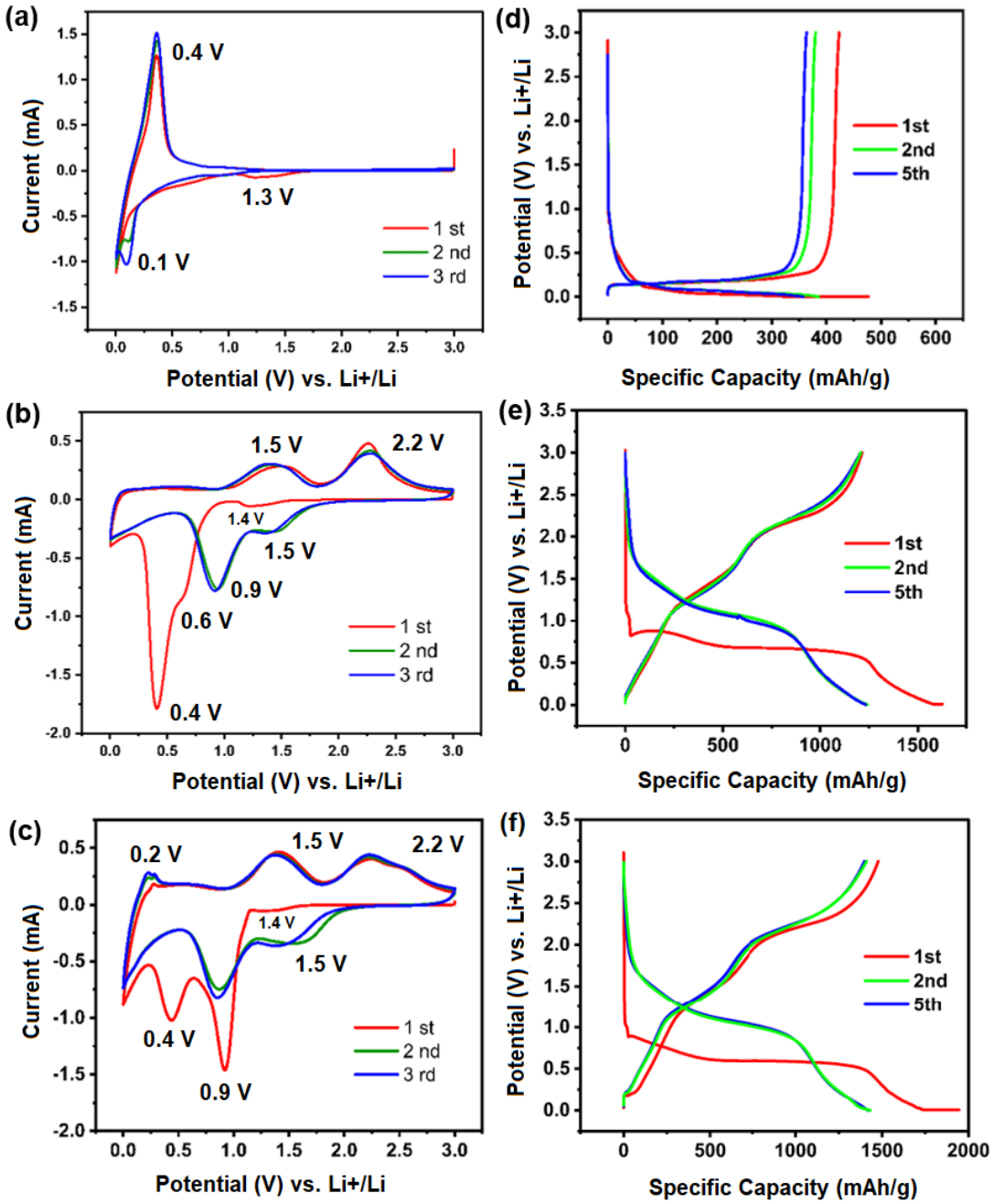

206

207 **Figure 4**. Cyclic voltammetry profiles: (a) EG, (b) NiO, and (c) NiO/GNF at a scan rate of 0.1
208 mV s^{-1} in the voltage range of 0.001–3.0 V. The discharge/charge profiles: (d) EG, (e) NiO,
209 and (f) NiO/GNF in the 1st, 2nd, and 5th cycles in the potential range of 0.001–3.0 V at 0.1 A
210 g^{-1}.

211 We tested the derived NiO-GNF as an anode in a two-electrode half-cell Lithium-ion
212 battery where Li foil acts as the counter electrode, and, for comparison, we tested pristine

expanded graphite and NiO **(Figure 4)**. The cyclic voltammetry (CV) measurements were conducted at the potential window between 0.001– 3 V (vs. Li^+/Li)) at a very slow scan rate of 0.1 mV s^{-1}. **Figure 4a- c** shows the first three CV cycles of the EG, NiO, and NiO-GNF. In the first cathodic scan (**Figure 4a**), EG displays a minor peak at ~1.3 V associated with the reductive destruction of the electrolyte and subsequent formation of a solid electrolyte interface (SEI).[30] The noticeable reduction at 0.1 V indicates the intercalation of lithium ions into a multilayer graphene.[31] At around 0.4 V, a sharp peak of oxidation corresponding to the de-intercalation of Li-ions from the LiC_x complex was observed.[31] In contrast, NiO and NiO/GNF share a few CV peaks in common, signifying the dominant contribution of NiO (**Figure 4b, c**). Both NiO and NiO-GNF exhibit a cathodic peak at 0.4 V vs. Li^+/Li, corroborating the irreversible formation of SEI and the reduction of NiO.[32] However, the peak is much stronger for pristine NiO compared to NiO-GNF, suggesting catalytic activity of NiO in electrolyte decomposition and an additional SEI layer formation.[33] In addition to the peak at 0.4 V, the first cathodic scans of NiO and NiO-GNF systems also show a reoccurring two oxidation peaks at 0.6/ 0.9 V and 1.4 V, respectively. This suggests the presence of NiO traces in both electrodes, which get reduced in the first cathodic scan.

The reduction process can be related to the conversation of NiO to metallic Ni and nickel suboxides ($NiO + 2Li^+ + 2e \rightarrow Ni + Li_2O$ + Ni suboxides).[10, 11] In addition, we noticed that the intensity of the peak at 0.9 V is much stronger and shifted in NiO-GNF compared to pristine NiO supporting an increased lithiation capacity. The enhanced capacity can be attributed to the intercalation of lithium with expanded graphitic sheets resulting in improved electrical conductivity and fast electron transfer kinetics.[34] The cathodic peak seen at 1.4 V in both systems has shifted towards a more positive potential of 1.5 V in subsequent cycles, which probably relates to the formation of various Ni suboxides during the first cycle.[10] The anodic oxidation peaks observed at 1.5 and 2.2 V in both NiO and NiO-GNF

systems can be related to the oxidation of Ni or Ni suboxides to NiO (Ni + Ni suboxides + Li_2O $\rightarrow$ NiO + $2Li^+$ + 2e). Additionally, a reoccurring mild oxidation plateau was observed only in the NiO/GNF system at 0.2 V, which might possibly be due to the de-intercalation of Li-ions in graphitic strctures.[12]

Figure 4d-f displays the galvanostatic charge/discharge curves recorded at a current density of 0.1 A g^{-1} after the 1st, 2nd, and 5th cycles. The EG samples display an initial discharge capacity of 476.8 mAh g^{-1} and a charge capacity of 423.1 mAh g^{-1}, resulting in initial Coulombic efficiency (ICE) of 88.7 %. The comparatively higher capacity of EG can be attributed to the improved electrical conductivity of expanded graphite nanoplatelets and enhanced ion storage due to enlarged interlayer spacing. Similarly, the initial discharge/charge capacities for the pristine NiO were 1626 mAh g^{-1} and 1214 mAh g^{-1}, respectively, and the ICE was 74.6 %. Compared to the NiO samples, NiO/GNF composite delivered a higher initial discharge/charge capacity of 1945/1477 mAh g^{-1} and an enhanced ICE of 76 %.

However, the capacity of the following discharge cycles of three LIBs was lower than that of the first cycle, which was associated with the SEI irreversibility and some undecomposed Li_2O phase, which agrees with the CV results. Furthermore, during the 5th cycle, NiO achieved a discharge/charge capacity of 1236/1207 mAh g^{-1} with an excellent Coulombic efficiency (CE) of 97.6 %. Similarly, the discharge/charge capacities of NiO-GNF were 1437 mAh g^{-1} and 1415 mAh g^{-1}, respectively, resulting in superior CE of 98.5 % due to the synergistic effect of NiO-GNF which was observed widely in previous studies.[10, 34] In addition, a significant capacitive contribution from expanded graphite can be expected due to increased interlayer distance. The 2nd and 5th discharge curves of NiO and NiO/GNF overlapped, suggesting more active material utilization over the cycling due to electrode conditioning.

We then evaluated the rate capability of the NiO-GNF electrode and compared it with EG and pristine NiO electrode, as shown in **Figure 5**. The NiO/GNF exhibits average capacities of 1429,1287,1148,1008, 821, and 752 mAh g^{-1} at current densities of 0.1, 0.2, 0.5, 0.8, 1, and 1.2 A $g^{-1,}$ respectively. The recorded capacities for the NiO-GNF electrode at different current densities were higher than those of EG and pristine NiO, revealing fast electrode kinetics resulting from the synergistic effect of NiO and graphitic nanomaterials (**Table S1**).[10, 34] When cycling at a current density of 0.1 A g^{-1}, the NiO-GNF electrode almost recovered its initial capacity, indicating excellent rate capability. In comparison, the NiO electrode recovered ~91.2 %, signifying the GNF backbone's role in enhancing the electrode's electrical conductivity and integrity. Further, the resultant capacity of 752 mAh g^{-1} at an ultra-high current density of 1.2 A g^{-1} was slightly higher than the theoretical capacity of NiO (i.e.,) 718 mAh g^{-1}. This further explains the NiO-GNF composite's excellent rate capability in the present work, which was significantly improved to the reported results such as NiO/RGO (564.5 mAh g^{-1}/ 0.8 A g^{-1})[10]; NiO/3D graphene (445 mAh g^{-1}/ 2 A g^{-1})[35]; NiO/graphene (~ 250 mAh g^{-1}, 1.5 A g^{-1})[25]; NiO/graphene NS (657 mAh g^{-1}, 1.436 A g^{-1})[36]; NiO /graphene form (210 mAh g^{-1}, 2 A g^{-1})[22] and graphene@NiO@ carbon (580 mAh g^{-1},1.6 A g^{-1})[37].

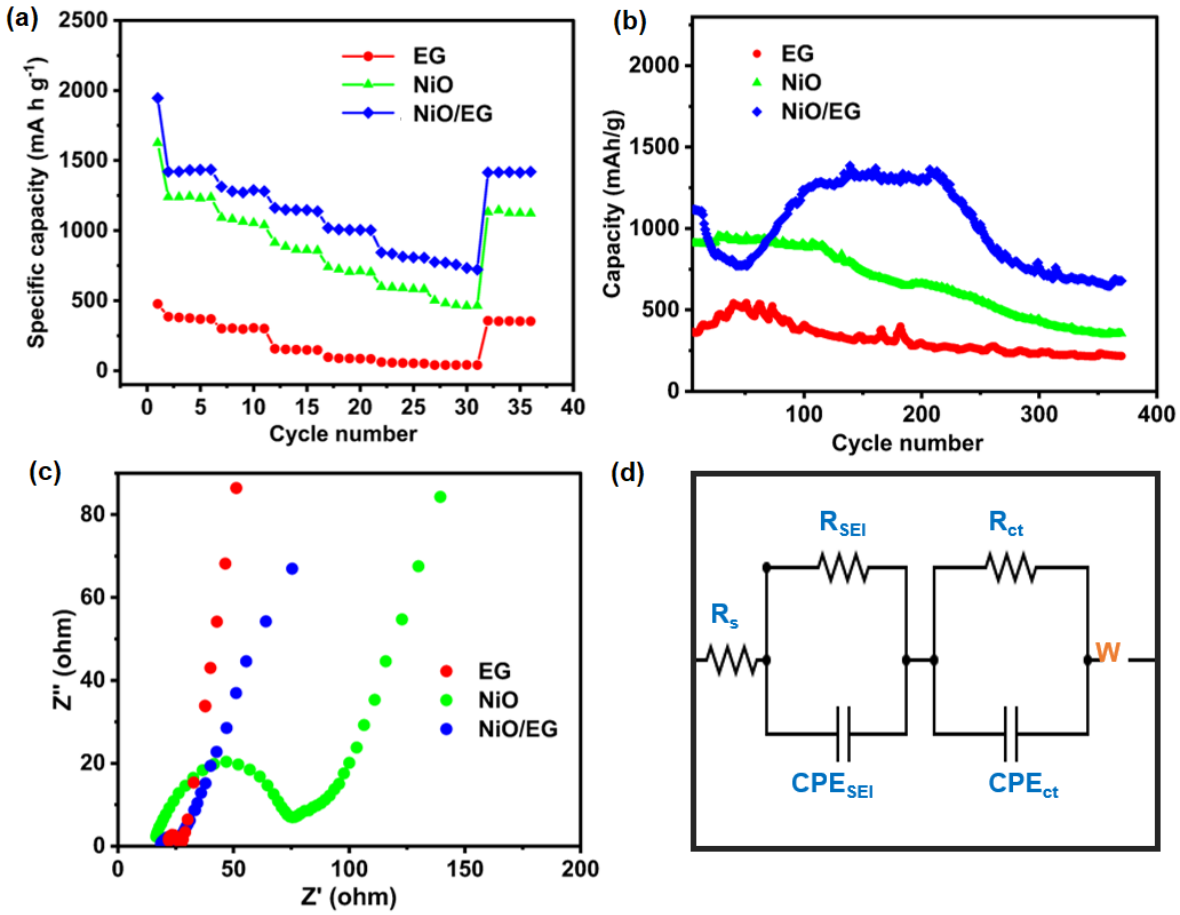

Figure 5. Lithium-ion battery performance of EG, NiO, and NiO-GNF. (a) Rate capability at different current densities, (b) Long-term cycling at 0.5 A g^{-1} in the potential range of 0.001–3.0 V, (c) The electrochemical impedance spectroscopy after the 5th cycle in the frequency range from 100 kHz to 0.01 Hz, and (d) The equivalent circuit of the cells used to simulate EIS curves.

We then evaluated the cyclic stability of the NiO/GNF electrode, which exhibited significantly higher stability than pristine NiO (See **Figure 5b)**. The composite electrode delivered a capacity of 678.2 mAh g^{-1} after 370 cycles at 0.5 A g^{-1}, corresponding to 60.7 % retention of its 6th cycle capacity. In comparison, the EG provided a capacity of 86.6 mAh g^{-1} after 370 cycles, whereas the pristine NiO experienced rapid capacity fade and delivered a capacity of 354 mAh g^{-1}. It is worth noting that the NiO-GNF electrode displayed four distinct stages in its cycling performance: initial capacity fading, a trend of increasing capacity from

approximately 50 to 100 cycles, capacity stabilization from around 100 to 220 cycles, and ultimately capacity fading until 370 cycles. Previous studies have observed the same cycling performance pattern for nickel oxides and their graphitic carbon composites over long term cycling.[38-41] The very first capacity decreasing trend could be attributed to the continuous formation of a solid-electrolyte interphase (SEI) layer on the anode surface and loss of Li ions as a result of anode activation. The second capacity increasing trend attributable to the enhanced Li- ions diffusion into the interior confines of the NiO-GNF composites, resulting in the exposure of new active sites for lithium-ion storage. The third period of capacity stabilization suggests the formation of a stable solid-electrolyte interphase (SEI) layer and that all available interior active sites have been successfully accessed, presenting a reversible Li-ion storage. The final capacity loss could be explained from following reasons: degradation and reformation of SEI layer, particle fractures and loss of anode active materials due to mechanical stress from continuous Li-ion insertion and extraction processes, Li dendrites formation, electrolyte decomposition and impedance growth.[42]

Additional explanations for these observations were drawn through electrochemical impedance spectroscopy (EIS). **Figure 5d** explains the equivalent circuit used to simulate the EIS results. The high-frequency intercept (R_s) symbolizes the electrolyte's ohmic resistance arising due to surface film formation. Correspondingly, the diameter of the semi-circle refers to the $R_{SEI,}$ the resistance due to the SEI layer, and R_{ct}, the charge-transfer resistance generates towards Li-ion at the electrode/electrolyte interface.[11] The depressed semicircles signify the presence of inhomogeneous surfaces; hence a constant phase element (CPE) is used in the equivalent circuit instead of a pure capacitance. Therefore, CPE_{SEI} and CPE_{ct} represent the SEI and double layer capacitance, respectively, and Warburg impedance W was attributed to Li-ion diffusion.[43, 44] The R_{ct} for NiO-GNF electrodes was very low as 0.636 Ω. In contrast, the resistance of NiO was considerably higher at 44.7 Ω **(Figure 5c)**. These observations

clearly demonstrate that NiO/GNF composite generates faster and better electrochemical kinetics with successful EG integration. Furthermore, the smaller semi-circle in NiO-GNF confirms the control pulverization of NiO and subsequent inhibition of additional SEI layer growth, validating the cyclic voltammetry results. In general, the electrochemical performances we have observed are encouraging when compared to recent findings on the application of NiO/carbon composites as anode material for Li-ion batteries **(Table S2).**

CONCLUSION

In summary, we explored a one-step hydrothermal synthesis approach for fabricating NiO-GNF composite material. During the hydrothermal process, the bulk graphitic particles transformed into expanded graphite nanosheets encapsulating the NiO nanoparticles within their carbon network. The chemical environment and surface morphology of the derived NiO-GNF composite materials was confirmed using several analytical techniques. Notably, the integration of expanded graphite with NiO nanostructures demonstrated significantly improved electrochemical performance, improved electrode integrity, enhanced Li-ion storage, and buffered electrode stress. The synergistic interaction between the expanded graphite and the NiO resulted in a 22.4 % capacity retention enhancement and a 324 mAh g^{-1} capacity improvement compared to the pristine NiO in the LIB application. To the best of our knowledge, the observed electrochemical performance of NiO-GNF, which was ~678.2 mAh g^{-1} at 0.5 A g^{-1} over 370 cycles, is a significant improvement compared to the reported carbon-based NiO composites. Overall, the derived material can be considered an excellent electrode due to its ease of synthesis, scalability, enhanced capacity retention, and long-term cyclability.

EXPERIMENTAL SECTION

Synthesis of NiO/GNF nanocomposite

Nickel sulfate hexahydrate, sodium acetate trihydrate, and trisodium citrate were purchased from Sigma Aldrich, UK. The natural flake graphite powder (100 mg, <1 mm) was dispersed in a 40 mL aqueous solution containing 0.2 mol dm^{-3} nickel sulfate hexahydrate,1 mol dm^{-3} sodium acetate trihydrate and 0.5 mol dm^{-3} trisodium citrate. The mixture was then transferred into a Teflon-lined stainless autoclave and heated at 200 °C for 20 h. The residue was thoroughly washed with de-ionized water and collected through vacuum filtration. Finally, the samples were heat treated at 350℃ for 12 h to convert hydrothermal intermediate hydroxide product into NiO. For comparison, NiO and EG were synthesized through the same approach.

Material characterization

The crystal structure of the samples was evaluated using a Rigaku D/Max Ultima II powder XRD with Cu Kα (λ = 0.154 nm) irradiation in the 2θ range of 20° to 80° at a scan rate of 0.02°. The surface morphology and elemental scans of the synthesized materials were evaluated using High-resolution field-emission scanning electron microscopy FEI Quanta 400F ESEM FEG operated at 20 kV, which was fitted with energy-dispersive X-ray spectroscopy (SEM-EDS). Raman measurements were carried out using a JY Horiba Lab RAM HR. A laser power of 28 μW was used as an excitation wavelength of 514 nm. All samples were gold-coated (~7nm) before analysis. The increase in interlayer spacing and EG formation was observed using a high-resolution transmission electron microscope (HRTEM, JEOL JEM-2100F, functioning at 200 kV) facilitated with EDX. X-ray photoelectron spectroscopy was employed to evaluate the chemical composition of the material. XPS analysis was carried out using a PHI Quantera X-ray photoelectron spectrometer with a chamber pressure of 5 × 10−9 Torr, and an Al cathode

was used as the X-ray source. The pass energies were set to 26.00 eV for the core-level scan, and the source power was set at 100 W. Thermogravimetric analysis (TGA) was performed on a TA Instrument- SDTQ600 under air with a heating rate of 10 °C min^{-1}. The Brunauer−Emmett−Teller (BET) technique calculated the materials' specific surface area and pore size distributions. The materials were evaluated using nitrogen sorption under 77.4 K by Autosorb iQ station 1 system. All samples were degassed at 200 °C for 12 h before the analysis.

Electrochemical measurements

The NiO-GNF composite's electrochemical performance was assessed using a 2032-type coin cell for lithium-ion batteries. In addition, a comparitive electrochemical analysis was performed for the NiO and EG separately. The slurry was prepared by mixing active material (70 wt. %), Super P (20 wt. %), and sodium carboxymethyl cellulose binder (10 wt. %, CMC, Sigma-Aldrich, 99%) and pasted on the copper current collector through the doctor blade technique. The electrodes were dried at 120 °C overnight in a vacuum oven (OV-11, Jeio Tech Co.) and punched into electrodes (d=13 mm) with an active materials mass loading over the electrodes ranging from 2 to 3 mg cm^{-2}. The LIB half cells were fabricated using a lithium foil (MTI Corp.) as a counter electrode, a glass microfiber filter (GF/B, pore size- 1.0 μm, Whatman) as a separator, and 1M Lithium hexafluorophosphate ($LiPF_6$) in ethylene carbonate: diethyl carbonate (1:1 vol.%) containing 2 % vinylene carbonate and 3% fluoroethylene carbonate (Solvionic, battery grade) as the electrolyte. The coin cells were assembled in a dry glove box under an argon atmosphere (Lab star eco, MBRAUN) with moisture and oxygen concentration below 1ppm. The cyclic voltammetry (CV) examinations of as-built coin cells were evaluated on an electrochemical workstation (Iviumstat, Ivium Technologies) within the potential range of 3.0 to 0.001 V (versus Li/Li^+) at a scan rate of 0.1 mV s^{-1}. Galvanostatic charge-discharge profiles and cycling performance were evaluated in the potential range of 3.0

to 0.001 V (vs. Li/Li+) at various current densities (Neware battery tester, BTS 4000). Electrochemical impedance spectroscopy (EIS) was measured over a frequency range of 0.01 Hz – 100 kHz with an amplitude of 5 mV.

REFERENCES

1. Asenbauer, J., et al., *The success story of graphite as a lithium-ion anode material–fundamentals, remaining challenges, and recent developments including silicon (oxide) composites.* 2020. **4**(11): p. 5387-5416.
2. Qin, D., et al., *Synthesis of hierarchical CoO nano/microstructures as anode materials for lithium-ion batteries.* 2014. **2014**.
3. Liu, C., et al., *Template free and binderless NiO nanowire foam for Li-ion battery anodes with long cycle life and ultrahigh rate capability.* 2016. **6**(1): p. 1-8.
4. Li, D., et al., *Facile synthesis of an Fe 3 O 4/FeO/Fe/C composite as a high-performance anode for lithium-ion batteries.* 2016. **6**(92): p. 89715-89720.
5. Li, J., et al., *Formation of dumbbell and sphere-like CuO as high-performance anode materials for lithium ion batteries.* 2020. **261**: p. 127058.
6. Ren, Y., et al., *Nanoparticulate TiO2 (B): an anode for lithium-ion batteries.* 2012. **124**(9): p. 2206-2209.
7. Huang, X., et al., *Porous ZnO nanosheets grown on copper substrates as anodes for lithium ion batteries.* 2011. **56**(14): p. 4960-4965.
8. Shao, J., et al., *Graphene aerogel encapsulated Fe-Co oxide nanocubes derived from Prussian blue analogue as integrated anode with enhanced Li-ion storage properties.* Applied Surface Science, 2019. **471**: p. 745-752.
9. Rahman, M.A., M.M. Rahman, and G.J.E.S. Song, *A review on binder-free NiO-Ni foam as anode of high performance lithium-ion batteries.* p. e278.
10. Li, X., et al., *Enhanced anode performance of flower-like NiO/RGO nanocomposites for lithium-ion batteries.* 2018. **217**: p. 547-552.
11. Chen, J., et al., *Enhanced lithium storage capability enabled by metal nickel dotted NiO–graphene composites.* 2019. **54**(2): p. 1475-1487.
12. Shi, W., et al., *Three-dimensional graphene sheets with NiO nanobelt outgrowths for enhanced capacity and long term high rate cycling Li-ion battery anode material.* Journal of Power Sources, 2018. **379**: p. 362-370.
13. Park, S.-H. and W.-J.J.R.A. Lee, *Coaxial carbon nanofiber/NiO core–shell nanocables as anodes for lithium ion batteries.* 2015. **5**(30): p. 23548-23555.
14. Li, T., et al., *Preparation of NiO–Ni/natural graphite composite anode for lithium ion batteries.* 2013. **553**: p. 167-171.
15. Mustansar Abbas, S., et al., *Facile synthesis of carbon nanotubes supported NiO nanocomposite and its high performance as lithium-ion battery anode.* Materials Letters, 2013. **107**: p. 158-161.
16. ZHANG, Y.-H., et al., *Synthesis of uniform nickel oxide nanoparticles embedded in porous hard carbon spheres and their application in high performance Li-ion battery anode materials.* 2015. **31**(2): p. 268-276.

17. Yuan, B., et al., *Investigation into electrochemical performance of NiO/graphene composite nanofibers synthesized by a simple method as anode materials for high-performance lithium ion batteries.* 2020. **7**(11): p. 115007.
18. Zhong, J., et al., *Ultrathin NiO nanoflakes perpendicularly oriented on carbon nanotubes as lithium ion battery anode.* 2013. **28**(18): p. 2577-2583.
19. Han, Q., et al., *Synthesis of one-dimensional PAN-based carbon fiber/NiO composite as an anode material for structural lithium-ion batteries.* 2020. **26**(12): p. 5935-5940.
20. Xiang, F., et al., *One-pot synthesis of MnO-loaded mildly expanded graphite composites as high-performance lithium-ion battery anode materials.* 2022. **897**: p. 163202.
21. Zhu, M., et al., *Prussian blue nanocubes supported on graphene foam as superior binder-free anode of lithium-ion batteries.* 2018. **749**: p. 811-817.
22. Shao, J., et al., *Facile synthesis of MOF-derived hollow NiO microspheres integrated with graphene foam for improved lithium-storage properties.* 2019. **784**: p. 869-876.
23. Cheng, G., Y. Yan, and R.J.N.J.o.C. Chen, *From Ni-based nanoprecursors to NiO nanostructures: morphology-controlled synthesis and structure-dependent electrochemical behavior.* 2015. **39**(1): p. 676-682.
24. Iskandar, F., et al., *Microwave-assisted reduction method under nitrogen atmosphere for synthesis and electrical conductivity improvement of reduced graphene oxide (rGO).* 2017. **7**(83): p. 52391-52397.
25. Kottegoda, I.R., et al., *Synthesis and characterization of graphene–nickel oxide nanostructures for fast charge–discharge application.* 2011. **56**(16): p. 5815-5822.
26. Fernando, N., et al., *Flexible free-standing Ni–Mn oxide antenna decorated CNT/nanofiber membrane for high-volumetric capacitance supercapacitors.* 2021. **13**(45): p. 19038-19048.
27. Liu, W., et al., *In situ fabrication of three-dimensional, ultrathin graphite/carbon nanotube/NiO composite as binder-free electrode for high-performance energy storage.* 2015. **3**(2): p. 624-633.
28. Huang, W., et al., *3D NiO hollow sphere/reduced graphene oxide composite for high-performance glucose biosensor.* 2017. **7**(1): p. 1-11.
29. Ye, S. and X.J.A.S. Guan, *HMT-controlled synthesis of mesoporous NiO hierarchical nanostructures and their catalytic role towards the thermal decomposition of ammonium perchlorate.* 2019. **9**(13): p. 2599.
30. Sivakkumar, S.R., J.Y. Nerkar, and A.G. Pandolfo, *Rate capability of graphite materials as negative electrodes in lithium-ion capacitors.* Electrochimica Acta, 2010. **55**(9): p. 3330-3335.
31. Zhong, M., et al., *Multilayer graphene spheres generated from anthracite and semi-coke as anode materials for lithium-ion batteries.* 2020. **198**: p. 106241.
32. Cao, Z. and B.J.F.i.M. Wei, *A facile route to metal oxides/single-walled carbon nanotube macrofilm nanocomposites for energy storage.* 2015. **2**: p. 40.
33. Wang, H.-q., et al., *In situ growth of NiO nanoparticles on carbon paper as a cathode for rechargeable Li–O 2 batteries.* 2017. **7**(38): p. 23328-23333.
34. Ou, J., et al., *Facile Preparation of NiO@ graphene Nanocomposite with Superior Performances as Anode for Li-ion Batteries.* 2022. **35**(2): p. 212-222.
35. Shi, W., et al., *Three-dimensional graphene sheets with NiO nanobelt outgrowths for enhanced capacity and long term high rate cycling Li-ion battery anode material.* 2018. **379**: p. 362-370.
36. Zou, Y. and Y.J.N. Wang, *NiO nanosheets grown on graphene nanosheets as superior anode materials for Li-ion batteries.* 2011. **3**(6): p. 2615-2620.
37. Wang, X., et al., *Growth of 3D hierarchical porous NiO@ carbon nanoflakes on graphene sheets for high-performance lithium-ion batteries.* 2016. **18**(5): p. 3893-3899.
38. Sun, X., et al., *Three-dimensionally "curved" NiO nanomembranes as ultrahigh rate capability anodes for Li-ion batteries with long cycle lifetimes.* 2014. **4**(4): p. 1300912.

39. Hu, N., Z. Tang, and P.K.J.R.a. Shen, *Hierarchical NiO nanobelt film array as an anode for lithium-ion batteries with enhanced electrochemical performance.* 2018. **8**(47): p. 26589-26595.
40. Hu, Q., et al. *Uniform NiO nanoparticles used as anodes in Li-ion batteries*. in *IOP Conference Series: Materials Science and Engineering*. 2019. IOP Publishing.
41. El Rouby, W.M.J.R.A., *Crumpled graphene: preparation and applications.* 2015. **5**(82): p. 66767-66796.
42. Edge, J.S., et al., *Lithium ion battery degradation: what you need to know.* 2021. **23**(14): p. 8200-8221.
43. Reddy, M.V., G.V. Subba Rao, and B.V.R. Chowdari, *Long-term cycling studies on 4V-cathode, lithium vanadium fluorophosphate.* Journal of Power Sources, 2010. **195**(17): p. 5768-5774.
44. Sakunthala, A., et al., *Energy storage studies of bare and doped vanadium pentoxide,(V 1.95 M 0.05) O 5, M= Nb, Ta, for lithium ion batteries.* 2011. **4**(5): p. 1712-1725.